On the effect of DCE MRI slice thickness and noise on estimated pharmacokinetic biomarkers – a simulation study

Jakub Jurek[1][0000−0003−4008−5267], Lars Reisæter[2][0000−0002−1242−1502], Marek Kociński[1,3][0000−0001−7088−4823], and Andrzej Materka[1][0000−0003−0864−1518]

[1] Institute of Electronics, Lodz University of Technology, Lodz, Poland
jakubjurekmail@gmail.com
[2] Department of Radiology, Haukeland University Hospital, Bergen, Norway
[3] Mohn Medical Image and Visualisation Center, Department of Biomedicine, University of Bergen, Bergen, Norway

Abstract. Simulation of a dynamic contrast-enhanced magnetic resonance imaging (DCE MRI) multiple sclerosis brain dataset is described. The simulated images in the implemented version have 1x1x1mm^3 voxel resolution and arbitrary temporal resolution. Addition of noise and simulation of thick-slice imaging is also possible. Contrast agent (Gd-DTPA) passage through tissues is modelled using the extended Tofts-Kety model. Image intensities are calculated using signal equations of the spoiled gradient echo sequence that is typically used for DCE imaging. We then use the simulated DCE images to study the impact of slice thickness and noise on the estimation of both semi- and fully-quantitative pharmacokinetic features. We show that high spatial resolution images allow significantly more accurate modelling than interpolated low resolution DCE images.

Keywords: DCE imaging · Quantitative DCE analysis · Semi-quantitative DCE analysis · Biomarkers.

1   Introduction

Dynamic contrast-enhanced magnetic resonance imaging (DCE-MRI) is a type of perfusion imaging. DCE can be used to assess tissue microcirculation parameters that are biomarkers for diagnosis, prognosis and treatment monitoring [6]. A DCE dataset is a time sequence of T1-weighted (T1W) MR images, acquired before, during and after administration of a paramagnetic contrast agent (CA).

DCE images are characterized, among others, by spatial and temporal resolution. The spatial resolution is defined as the ability to differentiate small structures in the image, while the temporal resolution refers to the time lapse between consecutive T1W scans. There exists a trade-off between the spatial and temporal resolution of DCE images. In general, as explained in [27], the decision concerning the acquisition of a high spatial resolution or a high temporal resolution dataset depends on the type of image analysis that is required (a

review of those can be found in [15]), which in turn depends on the disease or condition. The temporal resolution would be more important than spatial if the CA kinetics are to be finely studied. If tumour heterogeneity is to be studied, spatial resolution is more important than temporal. High spatial resolution of breast cancer MRI was shown to be critical by [9].

We claim that the trade-off between spatial and temporal resolution in DCE MRI can be improved, using super-resolution methodology, for example. The proof of the above claim requires demonstration of the feasibility of super-resolution methods, preferably using quantitative evaluation. In [14], we used MRI images of a physical phantom with known geometrical properties to quantitatively evaluate super-resolution images. For evaluation of super-resolution DCE images we postulate to use a digital phantom with known pharmacokinetics to simulate high spatial resolution DCE images.

According to our literature research, there have been just a few attempts in the past to simulate realistic DCE MRI data. Pannetier et al. [21] simulated a DCE experiment on the level of cells and microvessels. Abdominal DCE MRI simulation was studied in [2], using anatomy masks derived from CT images. Similarly, [7] simulated CA-based enhancement in a DCE sequence of the abdomen acquired without CA administration, using a mathematical model. In [3], prostate cancer DCE was simulated using an anatomical atlas of the prostate. These approaches used thick-slice images of the abdomen or prostate and thus resulted in low resolution (LR) simulated DCE images that are not suitable for evaluation of super-resolution DCE images. Simulation of higher resolution images was proposed by [4], which used a digital phantom of the brain, but did not model the partial volume effect (PVE), responsible for blurring and loss of spatial resolution. In this paper, we simulate DCE images by using the DCE signal modelling methods similar to [2, 7, 3] with a high resolution (HR) brain phantom published on BrainWeb: Simulated Brain Database [5], similarly as [4]. The BrainWeb phantom, however, has an important property that was not exploited in [4]: apart from having relatively high, isotropic spatial resolution, it is a fuzzy model with knowledge about the partial volume effect within each voxel. We innovate DCE image simulation by modelling the impact of PVE on enhancement curves in the high resolution isotropic simulated images and in thick-slice LR simulated images. We then conduct a study to estimate quantitative and semi-quantitative biomarkers from these images. We focus on the impact of slice thickness and noise on the value of the estimates.

2   Materials

2.1   Anatomical phantom of the brain

Construction of the adapted BrainWeb digital brain phantom is described in [5]. The phantom dataset is composed of 11 tissue maps of voxel resolution 1x1x1 mm^3. The value of voxels is in the [0,1] range and denotes the proportional contribution of a particular tissue to the voxel tissue content. The tissue classes and their parameters are summarized in Table 1. A sagittal slice through the

phantom image is shown in Figure 1, where each voxel has a label referring to the tissue with largest contribution[1].

Table 1: Tissue parameters of the brain phantom used for MRI simulation in [17]

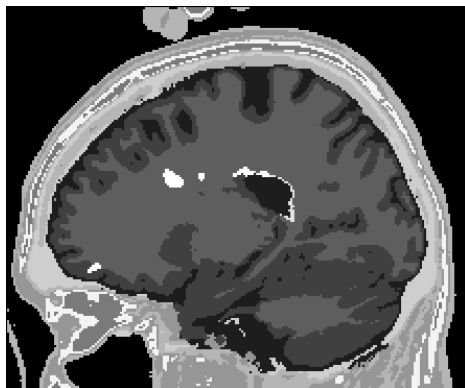| Parameter / Tissue class	background	cerebrospinal fluid	gray matter	white matter	glial matter	fat	muscle + skin	skin	skull	meat	MS lesions
T1	0	2569	833	500	833	350	900	2569	0	500	752
T2*	0	58	69	61	69	58	30	58	0	61	204
PD	0	1	0.86	0.77	0.86	1	1	1	0	0.77	0.76

Fig. 1: The BrainWeb phantom shown as a tissue-labelled sagittal slice

3   Methods

3.1   Modelling of CA concentration in blood plasma

The organs are supplied in blood by at least one artery. The model of the curve showing CA blood plasma concentration over time is called the arterial input function (AIF). Personalized models assume that the parameters of the AIF curve can be found by fitting the model to DCE timeseries taken from a large artery. Other models include population-based models, that are obtained by averaging of CA blood plasma contrast measurements of a group of subjects. A common population-based model is the Tofts biexponential model [25, 12], used for DCE simulation by [3]. The temporal resolution of the data that were used to fit the Tofts model, however, was several minutes [26]. This timescale does

---

[1] https://brainweb.bic.mni.mcgill.ca/tissue_mr_parameters.txt

not match the temporal resolution of modern DCE images. We therefore use the Parker AIF [22], given by

$$C_b(t) = \sum_{n=1}^{2} \frac{A_n}{\sigma_n \sqrt{2\pi}} \exp(-(t-T_n)^2)/2\sigma_n^2) + \alpha \exp(-\beta t)/(1 + \exp(-s(t-\tau)))$$

(1)

where the CA concentration in blood $C_b(t)$ is a parametrised sum of two Gaussians and an exponential modulated by a sigmoid function. The parameters were found in [22] by fitting the model to several DCE datasets and averaging: $A_1 = 0.809$ mMol $\cdot$ min, $A_2 = 0.330$ mMol $\cdot$ min, $T_1 = 0.17046$ min, $T_2 = 0.365$ min, $\sigma_1 = 0.0563$ min, $\sigma_2 = 0.132$ min, $\alpha = 1.05$ mMol, $\beta = 0.1685$ mMol, $s = 38.078$ min^{-1}, $\tau = 0.483$ min^{-1}. The AIF is shown in Figure 2.
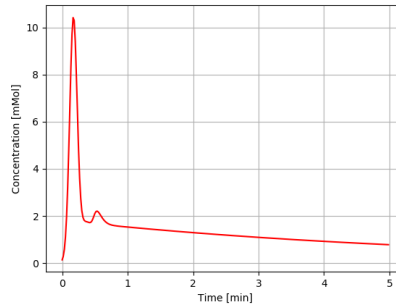

Fig. 2: The AIF assumed in our simulation, as proposed by Parker et al. [22]. Note that concentration peaks (first-pass- and recirculation-related) occur during the first minute of CA passage

3.2   Modelling of CA concentration in tissues

The concentration of the CA in tissues is described by the extended Tofts-Kety model:

$$C_p(t) = C_b(t)/(1-H) \tag{2}$$

$$C_t(t) = v_p C_p(t) + C_p(t) \otimes (K^{trans} e^{-k_{ep}t}) \tag{3}$$

Equation (2) calculates blood plasma CA concentration $C_p(t)$ using the blood hematocrit value $H = 0.42$ and CA concentration in blood $C_b(t)$. Then, Equation (3) calculates the tissue CA concentration $C_t(t)$ which is a sum of two components dependent on the plasma concentration, where $\otimes$ denotes convolution, K^{trans} is the volume transfer constant, k_{ep} is the efflux rate constant from

extravascular extracellular space to plasma and v_p is the blood plasma volume per unit volume of tissue, respectively [24, 19]. The latter three pharmacokinetic parameters are used to describe the state of the tissue and can reflect malignancy, blood-brain barrier (BBB) disruption etc.

3.3   From CA concentration to MR signal enhancement

In general, the MR signal in T1W MR images is related to both the T1 and T2* relaxation times of tissues. The CA creates chemical bonds with signal-generating molecules and changes the native T1 and native T2 times (T_{10} and T_{20}^*) by a factor related to the longitudinal and transverse relaxivities of the CA (R_1 and R_2) and the CA concentration in tissue. The contrast of the MR images is further dependent on the acquisition parameters set on the MR scanner: the echo time (TE), repetition time (TR) and flip angle (FA). Finally, scanner gain k and the density of protons in the tissue (PD) weigh the signal amplitude. Altogether, signal amplitude $S(t)$, in the commonly used spoiled gradient echo acquisition sequence that we adapt, is given by Equation (4), which we modified from [27, 3].

$$S(t) = k \cdot PD \cdot sin(FA) \cdot exp(-TE(\frac{1}{T_{20}^*} + R_2 C_t(t))) \cdot (1 - exp(-TR(\frac{1}{T_{10}} + R_1 C_t(t)))) \cdot$$
$$\cdot (1 - cos(FA) \cdot exp(-TR(\frac{1}{T_{10}} + R_1 C_t(t))))^{-1} \quad (4)$$

3.4   Modelling of PVE in high resolution voxels

Each voxel of an MR image represents a space in which a variety of tissues is present. These tissues have different PD value and relaxation times. For a particular voxel, its intensity in the image depends on the sum of signals sent by the mixture of tissues. Knowing the proportion of the tissues contributing to each voxel and the PD, we propose to calculate this sum using Equation (5):

$$S^v(t) = \sum_{l=1}^{11} \lambda_l^v \cdot k \cdot PD_l \cdot a_l(t) \quad (5)$$

where v is the index of the current voxel, l is the tissue class label and λ_l^v is the contribution of tissue l to voxel v. Using the above formula, PVE can be modelled for the original 1x1x1 mm^3-sized voxels of the HR phantom.

3.5   Modelling of thick-slice imaging

To model a low spatial resolution DCE imaging of the brain, we used an imaging model described in [14]:
$$I^{LR} = \mathbf{D}(I^{HR}) \quad (6)$$

where $\mathbf{D}$ is an operator leading to I^{LR}, a LR thick-slice anisotropic-voxel image and I^{HR} is the high resolution isotropic volume.

Operator $\mathbf{D}$ takes as input a block of $1 \times 1 \times AF$ neighbouring isotropic voxels (in the single, desired direction), calculates their average intensity and assigns it to the anisotropic output voxel, which covers the same space as the input voxel block. One can also view these operations as averaging AF thin slices to compute a single thick-slice. We refer to AF as the anisotropy factor.

Downsampling and averaging leads to an increased PVE and aliasing artifacts, deteriorating image quality [13]. As we will show, it also introduces errors to the estimates of pharmacokinetic parameters.

3.6   Modelling of noise

In DCE analysis, noise spoils not only the three spatial dimensions of the image, but also the fourth temporal dimension. In MRI generally, the noise has Rician distribution in high-intensity regions and Rayleigh distribution (a special case of the Rician) in background regions with no MR signal [10]. This situation can be modelled in the following way. Our simulated DCE images are noise-free, real-valued magnitude images, as follows from Equation (5). The intensity S_n^v of a noisy image voxel can be modelled as:

$$S_n^v = \sqrt{(S^v + N_R)^2 + (jN_I)^2} \qquad (7)$$

where j is the imaginary unit, N_R is the additive noise of the real part of the voxel signal and N_I is the additive noise of the complex part of the signal. This refers to the physical mechanism of image acquisition, as explained in [16], but the model can be used for our simulation as well. Both N_R and N_I are random, zero-mean Gaussian noise variables. Calculating the magnitude of the complex intensity in Equation ( ) gives images with the desired Rician noise distribution.

The level of noise is defined by the standard deviation of the Gaussians N_R and N_I, that is specified as a certain percentage of the intensity of the brightest tissue. In our experiment, we use 3% noise relative to the brightest tissue, which we find reasonable based on a comparison with a real brain DCE dataset.

3.7   Semi-quantitative DCE analysis

Semi-quantitative analysis of DCE timeseries is based on the paradigm of curve shapes [11, 8], that are believed to correspond to the presence and aggressiveness of neoplasms. This type of analysis does not require more than the DCE dataset itself to derive meaningful features. The features, as shown in Figure 3, are estimated from interpolated, normalized time-intensity curves and include time-to-peak, wash-in gradient and wash-out gradient, among others [11]. Time-to-peak is defined as the time necessary for the voxel signal to reach its maximum value $(t_3, S_{100\%})$. Wash-in gradient is the rate of change of the intensity starting at the timepoint where the intensity has 10% of the maximal value $(t_1, S_{10\%})$,

until it reaches 90% of the maximum value $(t_2, S_{90\%})$

$$G_{in} = \frac{t_2 - t_1}{S_{90\%} - S_{10\%}} \tag{8}$$

Wash-out gradient is defined as the rate of change of the intensity after time-to-peak until the end of the timeseries (t_4, S_{end}).

$$G_{out} = \frac{t_4 - t_3}{S_{end} - S_{100\%}} \tag{9}$$

Normalization of the curves is achieved by subtracting the mean value of the pre-injection signal from all time points and then dividing by the same mean value [11]. The injection time can be determined manually or automatically, while in our experiments it is known by design. For interpolation of the 6-second resolution simulated timeseries we used linear interpolation and subsampling by a factor of 60, thus obtaining the temporal resolution of 1/10 seconds for semi-quantitative analysis.

Semi-quantitative analysis seems to be more robust than fully quantitative analysis as demonstrated in [18]. We believe this is mainly due to the number of unknown variables in Equation 4. We shall leave investigation of this problem to another study.
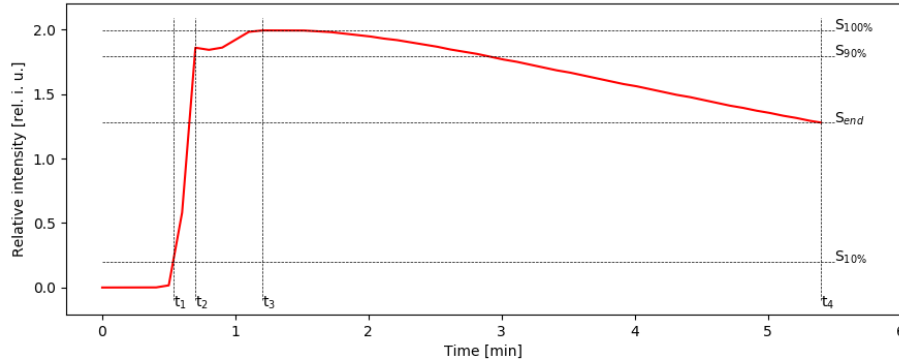

Fig. 3: Relevant times and relative signal intensity values for the determination of semi-quantitative pharmacokinetic parameters [11]

3.8 Fully quantitative DCE analysis

Fully quantitative analysis is a way to estimate the value of K^{trans}, k_{ep} and v_p parameters by fitting the function from Equation (3) to the measured time-intensity timeseries converted to time-concentration curves, for every voxel. To obtain the

time-concentration curves, it is not enough to acquire the DCE dataset. Conversion requires the estimation of the AIF for the analysed patient, which can be done in two ways. The first way is to use an averaged, population-based input function, such as the ones proposed by Orton [20] or Tofts-Weinmann [26, 25]. The advantage is that they are readily available, in contrast to personalized AIFs. To measure the latter, it is required to capture a large vessel in the image field-of-view. The size of the vessel is important due to smaller expected PVE in larger vessels, which leads to better AIF parameter estimation.

If the AIF is known, the remaining variables necessary to obtain the time-concentration curves are R_1, R_2, TE, TR, FA (known by design) and k, PD, T_{20}^* and T_{10} that still need to be estimated. The relaxation times can be estimated using multiple variable flip angle (VFA) acquisitions and appropriate signal equations [16]. However, it would be infeasible to extend scanning time in practice to estimate both T_{20}^* and T_{10}. The first of these appears in the term $exp(-TE(\frac{1}{T_{20}^*} + R_2C_t(t)))$ in (4). We obtain

$$exp(-TE(\frac{1}{T_{20}^*} + 0)) = exp(\frac{-TE}{T_{20}^*}) \qquad (10)$$

for $t = 0$ and

$$exp(-TE(\frac{1}{T_{20}^*} + R_2C_t(t))) = exp(\frac{-TE}{T_{20}^*}) \cdot exp(-TE \cdot R_2C_t(t)) \qquad (11)$$

for $t > 0$. The influence of (10) component on the total signal (4) can be neglected if TE is set to be short, given that T_{20}^* of tissues is longer than 30 ms [16, 27] (Table 1). Then, T_{10} is estimated by acquiring at least two T1-weighted datasets with a different FA, keeping the TR and TE constant. [27] suggests that $k \cdot PD$ and T_{10} can be fit to the signal equation, while we calculate it directly using only two VFA acquisitions. Then,

$$\frac{T_{10}}{TR} = log_e(\frac{S_1 sin(FA_2)cos(FA_1) - S_2 sin(FA_1)cos(FA_2)}{S_1 sin(FA_2) - S_2 sin(FA_1)})^{-1} \qquad (12)$$

where S_1 and S_2 are intensities of the two T1-weighted images and FA_1, FA_2 are two different flip angles. Once T_{10} is estimated, it can be used to calculate $k \cdot PD$ by solving Equation (4) for $t = 0$ and TE$>>$ T_{20}^*. With all the other parameters in hand, K^{trans}, k_{ep} and v_e can finally be estimated.

The latter yet requires conversion of the measured time-intensity signals to time-concentration signals. The relation is obtained from (4) and is the following:

$$C(t) = (TR + log_e(1 - kPDsin(FA)S^{-1}) - log_e(cos(FA)-$$
$$- kPDsin(FA)S^{-1})) \cdot (-R_1 T_{10} TR)^{-1} \quad (13)$$

We use a curve fitting approach to find the parameters of (3). The Levenberg-Marquardt algorithm was used to minimize the least squares error between the converted observed data and the model (3).

3.9 Implementation

All models were implemented in-house using Python and its popular libraries such as NumPy, SciPy, NiBabel, scikit-image and Matplotlib. Quantitative and semi-quantitative parameters were computed likewise. The programs were run on a laptop with an Intel Core i3-4000M CPU with 2.4 GHz clock speed and 16 GB of random access memory.

3.10 Simultion of high spatial resolution VFA and DCE images

Our simulated HR scanning session included acquisition of 56 image volumes in total. For most parameters of the acquisition, we followed the Quantitative Imaging Biomarkers Alliance 1.0 profile for DCE quantification [1]. The first VFA T_1-weighted image was simulated using FA = 15°, TR/TE = 4 ms/1 ms, scanner gain k was set to 10000 for all simulations. The DCE sequence was simulated using (5) for every voxel of the phantom, with TR/TE unchanged and FA = 25°. The first time-frame of the DCE sequence was used as the second VFA image for T_1-mapping, using (12). In total, the DCE sequence consisted of 55 volumes, 5 of which were pre-contrast ones. The simulated CA was gadopentate dimeglumine (Gd-DTPA) with $R_1 = 3.75$ (mM·s)$^{-1}$ and $R_2 = 4.89$ (mM·s)$^{-1}$[23]. The temporal resolution was set to 6 seconds, although the convolution in (3) was performed with signals of 1 second temporal resolution and the result was downsampled. For all tissues but the MS lesions, we set $K^{trans} = 0.0002$, $k_{ep} = 0.2$, $v_p = 0$. For MS lesions, which we assumed to be fully homogeneous, we set $K^{trans} = 0.01$, $k_{ep} = 1$, $v_p = 0.03$. The resulting ground-truth concentration curves for lesions and normal tissue are shown in Figure 4. Pre-contrast and post-contrast slices of the resulting DCE volumes are shown in Figure 5.
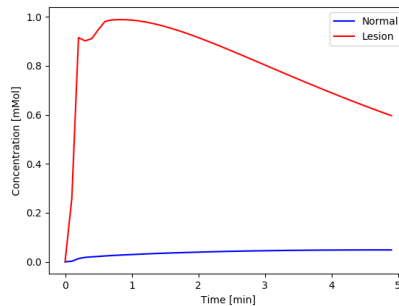

Fig. 4: Model-based pharmacokinetic curves representing CA concentration changes over time in normal (blue) and lesion (red) white matter (WM) tissue
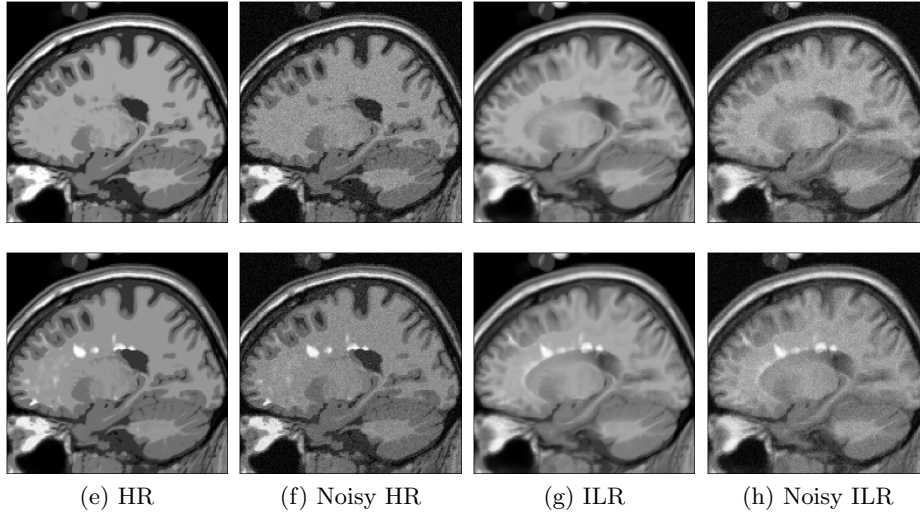
| (e) HR | (f) Noisy HR | (g) ILR | (h) Noisy ILR |

Fig. 5: Sample time-frames (pre-contrast – top, post-contrast – bottom) from simulated HR and interpolated LR (ILR) DCE images

3.11   Simulation of low spatial resolution DCE images

Low spatial resolution VFA volumes and DCE sequence were obtained from the HR counterparts using (6) with $AF = 6$. 3% noise was added to the volumes following LR imaging simulation. The LR images were then linearly interpolated to recover the original voxel resolution, although with a loss in the spatial resolution. As demonstrated in Figure 5, the ILR images are blurred in the plane of the slices and aliasing might occur in the direction perpendicular to the slices.

4   Results

4.1   Comparison of time-intensity signal curves in HR and LR DCE images

Curves sampled from a lesion region and from a healthy region are plotted in Figure 6. In the case of the healthy white matter, due to the protection of the BBB, only little enhancement is present. Since the sample was taken from a specific region where tissue is homogeneous, the noise-free curves do not differ. The noisy curves vary only due to the random noise.

A different result is observable for the curve sampled from a lesion. The noise-free curves are not identical in this case, because significant PVE occurs for the ILR volume. This has visible effect on the amount of enhancement and initial intensity value, as well as the slope of the curve in the initial wash-in and final wash-out phases. For actively enhancing lesion, noise is effectively smaller than

for the mildly enhancing normal white matter as compared to signal variations due to enhancement.

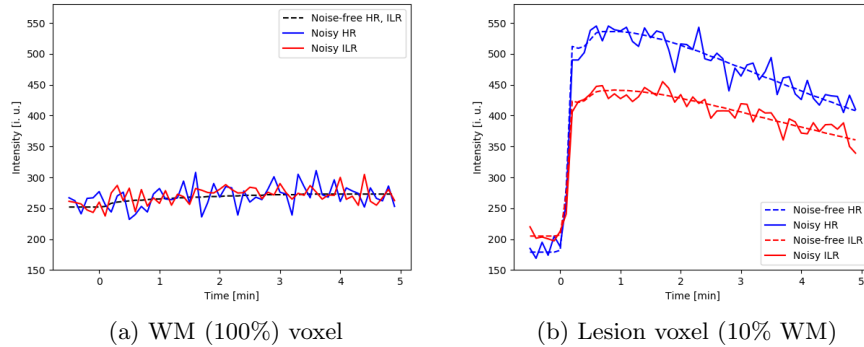(a) WM (100%) voxel   (b) Lesion voxel (10% WM)

Fig. 6: Sample intensity timeseries taken from noisy and noise-free HR and ILR images. In a), PVE does not occur due to tissue homogeneity and the difference in noisy curves is due to noise only. In b), PVE increases in the ILR image, affecting the curve shape

4.2   Semi-quantitative DCE analysis

In analysis of the simulated DCE datasets, we first performed semi-quantitative modelling. We estimated the time to peak and the mean and wash-out gradients for noise-free and noisy HR and ILR volumes, for all voxels were lesion tissue was dominant. Mean values and standard deviations of these estimates are presented in Table 2. The time to peak was slightly underestimated in the noise-free HR DCE. For other volumes, the value of this feature was overestimated, but the largest error and standard deviation is observed for the noisy ILR volume. For the wash-in gradient, its value was significantly underestimated for the noisy ILR DCE images, suggesting that is might be misleading to use it for diagnostic purposes. The wash-out gradient was overestimated by the noisy HR images, and for the noisy ILR images it was underestimated. The standard deviation of the latter was yet more than twice larger.

4.3   Fully quantitative DCE analysis

Estimates of K^{trans}, k_{ep} and v_p were obtained and then averaged over all voxels when the lesion tissue was dominant. The results are presented in Table 3. Comparison to the ground truth values reveals that noisy ILR volumes, which are designed to be the most similar to actual DCE datasets, are associated with

Table 2: Mean and standard deviation of the semi-quantitative pharmacokinetic parameters in voxels where MS lesion tissue is dominant. See Section 3.7 for equations

Image Volume	t_3 [min]		G_{in} [min^{-1}]		G_{out} [min^{-1}]	
	mean	st. dev.	mean	st. dev.	mean	st. dev.
HR	1.28	0.07	7.31	1.75	-0.13	0.03
HR + 3% N	1.60	0.43	4.12	2.80	-0.17	0.05
ILR	1.61	0.30	3.44	2.27	-0.06	0.04
ILR + 3% N	1.91	0.73	1.77	1.85	-0.11	0.10
MS lesion value	1.3	-	8.55	-	-0.14	-

the largest standard deviation of the estimates. The errors in the mean values are also largest for the ILR images. It is worth noting that even the HR volumes resulted in estimates relatively far from the ground truth values.

Table 3: Mean and standard deviation of the quantitative pharmacokinetic parameters in voxels where MS lesion tissue is dominant. See Section 3.2 for explanation of the parameters

Image Volume	K^{trans} [10^{-3}·min^{-1}]		k_{ep} [min^{-1}]		v_p	
	mean	st. dev.	mean	st. dev.	mean	st. dev.
HR	6.9	1.5	0.96	0.03	0.019	0.004
HR + 3% N	7.1	3.1	0.97	0.08	0.018	0.008
ILR	3.7	1.8	0.84	0.10	0.012	0.005
ILR + 3% N	3.5	2.5	0.86	0.20	0.009	0.015
MS lesion value	10	-	1	-	0.03	-

5   Discussion and conclusions

The results clearly show the negative impact of the PVE on estimation of both semi- and fully-quantitative pharmacokinetic features in voxels where lesion tissue is dominant. Although we have simulated a brain dataset with multiple sclerosis, as allowed by the publicly available anatomical data, we think that similar results would be obtained for other organs and other lesion types. Therefore, the main point of our work is to acknowledge the opinions that spatial resolution is the crucial factor in DCE analysis, regardless of the analysis type. It is also clear that magnitude of errors is feature-dependent. In our analysis, time to peak appeared to be estimated with lower error than wash-in gradient, for example. The reason could be that averaging and downsampling, which is the source of spatial resolution loss in ILR DCE images, affect different parts of the time-intensity curves to a variable degree.

3% noise that was added to HR and LR images showed to have smaller impact on the estimates of fully quantitative parameters than 6 mm slice thickness. For semi-quantitative parameters, this effect was not so clear. The estimate of t_3 and G_{in} was affected to a similar degree by noise and slice thickness. However, for the G_{out} parameter, noise lead to overestimation of the negative slope, while slice thickness cause underestimation. Both noise and slice thickness increased the standard deviation of the estimate. This is understandable for random noise. For slice thickness, it implies that different voxels are affected to a variable degree by averaging and downsampling leading to thick slices.

Considering possible drawbacks of our study, we first note that our DCE simulations are based on imaging and perfusion models that do not reflect the complex phenomena of both image acquisition and pharmacokinetics perfectly. In our experiment, HR image acquisition was simulated using signal equations and LR image acquisition was modelled using averaging and downsampling. Both models simplify the complex nature of MR imaging and MR signal measurements and do not reflect all phenomena that occur during imaging. The pharmacokinetic model of Tofts-Kety that we used to simulate the CA kinetics is a popular, but again simplified description of the true, complex processes of CA passage through vessels and tissues. The anatomical model of the brain is simplified as well, it does not include vessels, for example. Lesions were modelled as homogeneous regions, while in reality, they are heterogeneous. Nonetheless, we believe that the above simplifications do not hinder our goals of studying the influence of spatial resolution on DCE image analysis results, since this analysis always assumes some simplifications. Moreover, this influence might be common to various models, as it basically results from signal sampling theory. We find the simulated images useful to study the influence of such factors as noise or PVE on the biomarkers computed from the images. In the future, it is possible to use more complicated models of the imaging process and CA kinetics to improve the realisticness of the simulated DCE dataset. To the best of our knowledge, however, we are first to simulate DCE images with adjustable slice thickness, noise and such that incorporate the partial volume effect. Such images can be of great use in future studies, for example for assessment of super-resolution methods or pharmacokinetic modelling methods, since they allow a truly quantitative evaluation when kinetic feature values are known by design.

We have successfully simulated DCE MRI images using brain anatomy. We used them to study the impact of spatial resolution on pharmacokinetics-related biomarkers, which revealed the lacks of typical DCE images, which usually have considerable slice thickness.

Acronyms

AIF - arterial input function, BBB - blood-brain barrier, CA - contrast agent, DCE MRI - dynamic contrast-enhanced magnetic resonance imaging, FA - flip angle, Gd-DTPA - gadopentate dimeglumine, HR - high resolution, ILR - interpolated low resolution, LR - low resolution, PD - proton density, PVE - partial

volume effect, TE - time to echo, TR - repetition time, T1W - T1-weighted, VFA - variable flip angle, WM - white matter

References

1. Profile: DCE MRI quantification (2012), http://qibawiki.rsna.org/index.php/Profiles
2. Banerji, A.: Modelling and simulation of dynamic contrast-enhanced MRI of abdominal tumours. Ph.D. thesis (2012)
3. Betrouni, N., Tartare, G.: Prostateatlas simdce: A simulation tool for dynamic contrast enhanced imaging of prostate. IRBM **36**(3), 166–169 (2015)
4. Bosca, R.J., Jackson, E.F.: Creating an anthropomorphic digital MR phantom—an extensible tool for comparing and evaluating quantitative imaging algorithms. Physics in Medicine & Biology **61**(2), 974 (2016)
5. Collins, D.L., Zijdenbos, A.P., Kollokian, V., Sled, J.G., Kabani, N.J., Holmes, C.J., Evans, A.C.: Design and construction of a realistic digital brain phantom. IEEE transactions on medical imaging **17**, 463–468 (Jun 1998). https://doi.org/10.1109/42.712135
6. Cuenod, C.A., Balvay, D.: Perfusion and vascular permeability: basic concepts and measurement in DCE-CT and DCE-MRI. Diagnostic and interventional imaging **94**, 1187–1204 (Dec 2013). https://doi.org/10.1016/j.diii.2013.10.010
7. Dikaios, N., Arridge, S., Hamy, V., Punwani, S., Atkinson, D.: Direct parametric reconstruction from undersampled (k, t)-space data in dynamic contrast enhanced MRI. Medical image analysis **18**(7), 989–1001 (2014)
8. Fabijańska, A.: A novel approach for quantification of time-intensity curves in a DCE-MRI image series with an application to prostate cancer. Computers in biology and medicine **73**, 119–130 (Jun 2016). https://doi.org/10.1016/j.compbiomed.2016.04.010
9. Furman-Haran, E., Grobgeld, D., Kelcz, F., Degani, H.: Critical role of spatial resolution in dynamic contrast-enhanced breast MRI. Journal of magnetic resonance imaging : JMRI **13**, 862–867 (Jun 2001). https://doi.org/10.1002/jmri.1123
10. Gudbjartsson, H., Patz, S.: The rician distribution of noisy MRI data. Magnetic resonance in medicine **34**, 910–914 (Dec 1995). https://doi.org/10.1002/mrm.1910340618
11. Haq, N.F., Kozlowski, P., Jones, E.C., Chang, S.D., Goldenberg, S.L., Moradi, M.: A data-driven approach to prostate cancer detection from dynamic contrast enhanced MRI. Computerized medical imaging and graphics : the official journal of the Computerized Medical Imaging Society **41**, 37–45 (Apr 2015). https://doi.org/10.1016/j.compmedimag.2014.06.017
12. He, D., Xu, L., Qian, W., Clarke, J., Fan, X.: A simulation study comparing nine mathematical models of arterial input function for dynamic contrast enhanced MRI to the parker model. Australasian physical & engineering sciences in medicine **41**, 507–518 (Jun 2018). https://doi.org/10.1007/s13246-018-0632-0
13. Jurek, J.: Super-resolution reconstruction of three dimensional magnetic resonance images using deep and transfer learning. Ph.D. thesis (2020)
14. Jurek, J., Kociński, M., Materka, A., Elgalal, M., Majos, A.: CNN-based super-resolution reconstruction of 3D MR images using thick-slice scans. Biocybernetics and Biomedical Engineering **40**(1), 111–125 (2020)
15. Khalifa, F., Soliman, A., El-Baz, A., Abou El-Ghar, M., El-Diasty, T., Gimel'farb, G., Ouseph, R., Dwyer, A.C.: Models and methods for analyzing DCE-MRI: a review. Medical physics **41**, 124301 (Dec 2014). https://doi.org/10.1118/1.4898202

16. Kwan, R.K., Evans, A.C., Pike, G.B.: MRI simulation-based evaluation of image-processing and classification methods. IEEE transactions on medical imaging **18**, 1085–1097 (Nov 1999). https://doi.org/10.1109/42.816072

17. Kwan, R.K.S., Evans, A.C., Pike, G.B.: An extensible MRI simulator for post-processing evaluation. Visualization in Biomedical Computing (Jan 1996). https://doi.org/10.1007/BFb0046947, http://dx.doi.org/10.1007/BFb0046947

18. van der Leij, C., Lavini, C., van de Sande, M.G.H., de Hair, M.J.H., Wijffels, C., Maas, M.: Reproducibility of DCE-MRI time-intensity curve-shape analysis in patients with knee arthritis: A comparison with qualitative and pharmacokinetic analyses. Journal of magnetic resonance imaging : JMRI **42**, 1497–1506 (Dec 2015). https://doi.org/10.1002/jmri.24933

19. O'Connor, J., Tofts, P., Miles, K., Parkes, L., Thompson, G., Jackson, A.: Dynamic contrast-enhanced imaging techniques: Ct and mri. The British journal of radiology **84**(special_issue_2), S112–S120 (2011)

20. Orton, M.R., d'Arcy, J.A., Walker-Samuel, S., Hawkes, D.J., Atkinson, D., Collins, D.J., Leach, M.O.: Computationally efficient vascular input function models for quantitative kinetic modelling using DCE-MRI. Physics in medicine and biology **53**, 1225–1239 (Mar 2008). https://doi.org/10.1088/0031-9155/53/5/005

21. Pannetier, N.A., Debacker, C.S., Mauconduit, F., Christen, T., Barbier, E.L.: A simulation tool for dynamic contrast enhanced MRI. PloS one **8**, e57636 (2013). https://doi.org/10.1371/journal.pone.0057636

22. Parker, G.J.M., Roberts, C., Macdonald, A., Buonaccorsi, G.A., Cheung, S., Buckley, D.L., Jackson, A., Watson, Y., Davies, K., Jayson, G.C.: Experimentally-derived functional form for a population-averaged high-temporal-resolution arterial input function for dynamic contrast-enhanced MRI. Magnetic resonance in medicine **56**, 993–1000 (Nov 2006). https://doi.org/10.1002/mrm.21066

23. Reichenbach, J., Hackländer, T., Harth, T., Hofer, M., Rassek, M., Mödder, U.: 1H T1 and T2 measurements of the MR imaging contrast agents Gd-DTPA and Gd-DTPA BMA at 1.5 T. European radiology **7**(2), 264–274 (1997)

24. Tofts, P.S.: Modeling tracer kinetics in dynamic Gd-DTPA MR imaging. Journal of magnetic resonance imaging : JMRI **7**, 91–101 (1997). https://doi.org/10.1002/jmri.1880070113

25. Tofts, P.S., Kermode, A.G.: Measurement of the blood-brain barrier permeability and leakage space using dynamic MR imaging. 1. fundamental concepts. Magnetic resonance in medicine **17**(2), 357–367 (1991)

26. Weinmann, H.J., Laniado, M., Mützel, W.: Pharmacokinetics of GdDTPA/dimeglumine after intravenous injection into healthy volunteers. Physiological chemistry and physics and medical NMR **16**(2), 167–172 (1984)

27. Yankeelov, T., Gore, J.: Dynamic contrast enhanced magnetic resonance imaging in oncology:theory, data acquisition,analysis, and examples. Current Medical Imaging Reviews **3**(2), 91–107 (may 2009). https://doi.org/10.2174/157340507780619179